The Astrophysical Journal, 829:131 (11pp), 2016 October 1 doi:10.3847/0004-637X/829/2/131

RELEASE HISTORY AND TRANSPORT PARAMETERS OF RELATIVISTIC SOLAR ELECTRONS INFERRED FROM NEAR-THE-SUN IN SITU OBSERVATIONS

N. Agueda[1] and D. Lario[2]
[1] Department Física Quàntica i Astrofísica, Institut de Ciències del Cosmos (ICCUB), Universitat de Barcelona, Martí i Franquès 1, E-08028, Barcelona, Spain
[2] The Johns Hopkins University, Applied Physics Laboratory, Johns Hopkins Road 11100, Laurel, MD 20723, USA
Received 2016 May 10; revised 2016 July 14; accepted 2016 July 14; published 2016 September 29

ABSTRACT

We study four consecutive 300–800 keV electron events observed on 1980 May 28 by *Helios-1*, when the spacecraft was located at 0.31 au from the Sun. We use two different techniques to extract the release time history of electrons at the Sun: (1) a data-driven method based on the assumption that particles conserve their magnetic moment as they propagate between the Sun and the spacecraft and (2) an inversion method that utilizes particle transport simulation results. Both methods make use of the particle angular distributions measured relative to the local direction of the magnetic field. The general characteristics of the release time profiles obtained by these two techniques are similar, especially during their rising phases. We find indications that the strength of the interplanetary scattering varies with the size of the solar parent event, suggesting that scattering processes are not necessarily an inherent property of the medium but are related to the amount of released particles at the Sun. We use the inferred release profiles to compute the expected intensities at 1 au. In contrast to simultaneous near-Earth observations by the *Interplanetary Monitoring Platform* (*IMP-8*), our simulations predict the observation of four separate events at 1 au. Processes that could contribute to the observation of one single time-extended event at 1 au include (1) distinct magnetic connections of the spacecraft to the particle sources, (2) the spatio-temporal evolution of the particle sources, and (3) different particle transport conditions, including a variation of λ_r with radial distance and/or heliolongitude, as well as the possibility that electrons reached *IMP-8* by diffusion perpendicular to the interplanetary magnetic field.

Key words: Sun: activity – Sun: heliosphere – Sun: particle emission

1. INTRODUCTION

Solar energetic particle (SEP) events observed in interplanetary space present a large variability in terms of intensity, composition, and spatial and temporal extent (e.g., Kahler et al. 1999; von Rosenvinge & Cane 2006; Gopalswamy 2012). In particular, the observed SEP intensity time profiles result from both (i) the injection history of SEPs as they are released from their acceleration sites, and (ii) the transport processes undergone by the particles as they travel through the interplanetary medium from their sources to the particle detectors on board spacecraft. The transport effects pose the main difficulty in reconstructing the processes of particle release occurring at the Sun from in situ spacecraft observations. In order to correctly extract interplanetary transport effects, an effective treatment of the SEP transport processes in the heliosphere is required. Several approaches have been used over the years to characterize the SEP transport conditions (e.g., Reid 1964; Earl 1974, 1976; Roelof 1975, 1979, 2008; Hamilton 1977; Beeck et al. 1987; Kallenrode et al. 1992; Ruffolo 1995; Kocharov et al. 1998; Ruffolo et al. 1998; Laitinen et al. 2000, 2013; Dröge 2003; Qin et al. 2005; Wang et al. 2006; Agueda et al. 2008, and references therein). Such approaches allow us to reproduce spacecraft SEP observations and thereby infer SEP injection histories. The particle angular distributions relative to the local direction of the magnetic field (i.e., pitch-angle distributions (PADs)) have proven to be relevant in these analyses. A given intensity time profile can be fitted using a large variety of combinations of the injection profile at the Sun and interplanetary transport conditions, although this non-uniqueness can be constrained by a simultaneous analysis of the omni-directional intensity and the computed anisotropy time profiles (e.g., Schulze et al. 1977). More recently this problem has been further constrained by including the most direct form of data in the analysis, that is, the measured directional distributions together with the angular response of the detector (Agueda et al. 2008, 2009a, 2014).

The observation of SEP events by spacecraft located at heliocentric distances smaller than 1 au (i.e., closer to the acceleration site), is essential to understand the mechanisms of SEP acceleration and release (e.g., McComas et al. 2007). The science goals of the next generation of spacecraft traveling close to the Sun (i.e., Solar Orbiter and *Solar Probe Plus*) include the exploration of the mechanisms that accelerate and transport energetic particles (Fox et al. 2015) as well as the study of how energetic particles are released from their sources and distributed in space and time (Müller et al. 2013).

The two pioneering *Helios* spacecraft explored the inner heliosphere (from 0.29 to 0.98 au) during solar cycle 21 and captured several SEP events during their fast perihelion passages. In this work, we revisit a sequence of four consecutive relativistic electron events observed by *Helios-1* at 0.31 au on 1980 May 28 with analysis techniques that were unavailable during the *Helios* era. Relativistic electrons were also observed by the *Interplanetary Monitoring Platform* (*IMP-8*), which was located in the Earth's magnetosheath on 1980 May 28. In contrast to *Helios-1* observations, *IMP-8* detected only a single extended particle intensity enhancement; i.e., *IMP-8* did not resolve four individual events. Wibberenz & Cane (2006) suggested that the source of the events seen by *Helios*-1 and *IMP-8* was the same and that the main difference between the two profiles was caused primarily by the different radial positions of the two spacecraft and the more prominent role of interplanetary scattering further away from the Sun. These events were originally considered by Kallenrode &

Table 1
Solar Flares Associated with the Origin of the SEP Events

Event #	Soft X-Ray Flare				Hα Flare	
	Start	End	Max	Class	Class	Location
1	15:53	16:19	15:58	C9.1	SN	S24W28
2	17:05	17:53	17:18	M3.6	1B	S18W35
3	19:24	20:53	19:51	X1.1	2B	S18W33
4	23:32	24:45	23:44	M6.9	2B	S17W39

Wibberenz (1991) to infer the SEP injection histories, although only the second event of the series was discussed in detail. In that work, the time history of the release of energetic particles at the Sun was obtained by simply shifting the observed intensity time profile by the ballistic travel time of the particles along a smooth interplanetary magnetic field (IMF) line considered to be an Archimedean spiral.

Here, we apply two independent techniques to extract the release time history of the observed relativistic solar electrons and their interplanetary transport conditions. Both techniques rely on the information provided by the reconstructed PADs at the spacecraft location. We compare the release histories provided by both techniques. In Section 2 we present the observations of these four SEP events. In Section 3 we describe the techniques used to determine the release time histories of relativistic electrons at the Sun and their interplanetary transport parameters. In Section 4 we compare the injection histories inferred for each event. In Section 5 we discuss the results in a broader context and analyze the differences between the *Helios* and the *IMP-8* SEP events. Finally, Section 6 summarizes the main conclusions of the work and the utility of these techniques in interpreting the observations that the upcoming missions *Solar Orbiter* and *Solar Probe Plus* will perform.

2. OBSERVATIONS

On 1980 May 28 *Helios-1* was located at 0.31 au from the Sun and ∼5°–8° ahead (west) of Earth. A series of homologous flares from NOAA Active Region #2470 or Hale Plage Region 16864 occurred on that day (Gaizauskas 1983). Table 1 lists the start, end, and peak times of the soft X-ray (SXR) emission and the X-ray class of the flares associated with the origin of the four SEP events as observed by *GOES-3*. Table 1 also lists the Hα class and location of the flares as seen from Earth.[3] We refer the reader to Gaizauskas (1983) for a detailed description of the characteristics of the flaring regions and a list of the radio phenomena observed in association with such flares (see their Table 2). The configuration of the Sun, flare region, and *Helios-1* during this period is shown in Figure 1. We plot nominal magnetic field lines connecting each spacecraft with the Sun, assuming a Parker spiral IMF configuration considering the solar wind speed measured in situ during the time interval when the SEP events were observed (∼250 km s^{-1} for *Helios*-1 and ∼275 km s^{-1} measured by *IMP-8* exiting the magnetosheath). The footpoints of the nominal IMF lines connecting Earth with the Sun was located at a longitude close to the west limb of the Sun (∼W89°), i.e., poorly connected to the sites of the flares. By contrast, *Helios-1* was much better connected to

[3] https://www.ngdc.noaa.gov/stp/space-weather/solar-data/solar-features/solar-flares/x-rays/goes/

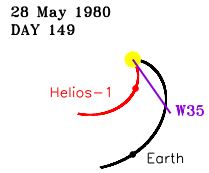

Figure 1. View from the north ecliptic pole showing the location of *Helios-1* (red symbol) and *IMP-8* (black symbol) on day 149 of 1980 (1980 May 28). Nominal interplanetary magnetic field lines are shown connecting each spacecraft with the Sun (yellow circle at the center, not to scale) considering the solar wind speed measured during the SEP events. The purple line indicates the longitude of the parent active region at the time of the second event (W35 as seen from Earth).

the flare sites (close to ∼W30°, as seen from Earth). The purple line in Figure 1 identifies the longitude of the solar flare (W35) associated with the origin of the second electron event.

Figure 2 shows the four distinct electron events observed by *Helios-1* in association with the four flares listed in Table 1. Figure 2(a) shows 300–800 keV electron intensities as measured in each one of the eight sectors of the E03 channel of the E6 (University of Kiel) instrument on board *Helios-1* (Kunow et al. 1977). Monte Carlo simulations of the E6 instrument response (Bialk et al. 1991) showed that the E03 channel may also respond to (1) protons mostly in the energy range ∼4–13 MeV with response efficiencies smaller than ∼10%–15% at most, and (2) electrons of energy higher than its nominal energy range, being the peak in response at 950 keV. For the four events under study, the electron fluxes were several orders of magnitude higher than the proton fluxes (not shown here) and evolved differently suggesting that possible proton contamination into the E03 channel was minimal. Similarly, particle intensities measured in the next nominal electron channel (i.e., E08 with nominal energy window 0.8–2 MeV) were much lower than the intensity in the E03 channel (not shown here) suggesting a very steep energy spectrum. We also studied the effect of the energy response of the E03 channel computed by Bialk et al. (1991) on the intensities observed at 0.31 au. We used an interplanetary transport model (Agueda et al. 2008) to compute synthetic electron intensities expected at 0.31 au for energies from 300 keV to 5 MeV. Assuming the energy response computed by Bialk et al. (1991; see their Figure 3), we found that the observed intensities would be smaller than the intensities expected assuming the nominal 300–800 keV energy range, since in the first case the instrument would respond more to higher energy electrons, for which there are lower intensities. The effect depends on the spectral index of the source, being the intensities up to two orders of magnitude lower for very steep energy spectra ($\gamma = 5$). On the other hand, the time evolution of the intensities in both cases, assuming either 300–800 keV or the Bialk et al. (1991) extended energy range, agree within the time resolution considered in this study (one minute). Therefore, we will use 300–800 keV as the nominal energy window of the E03 channel with the caveat that the inferred release time profiles might be underestimated by up to two orders of magnitude.

The spin axis of *Helios-1* was perpendicular to the ecliptic plane so that E6 was able to scan different regions of the ecliptic plane as the spacecraft rotated (in eight equally spaced sectors). The insert on the bottom right corner of Figure 2(a) shows the orientation of the eight sectors of E6 with respect to the Sun. During the onset and peak of the events the electron

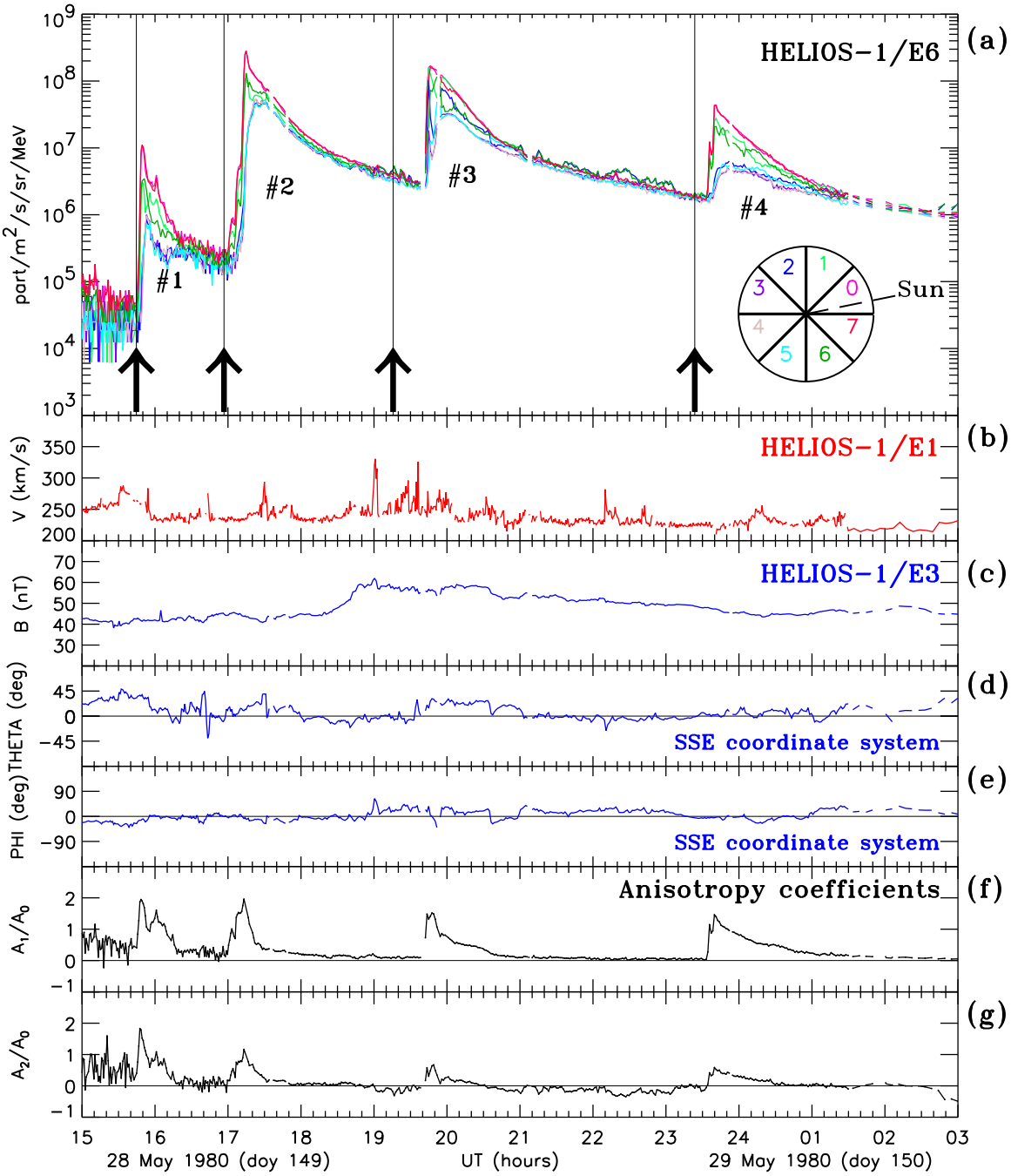

Figure 2. (a) One-minute averages of the 300–800 keV electron intensities as measured in the eight sectors of E6 on board *Helios-1*. The four electron events have been identified with the numbers #1 to # 4. (b) 45 s measurements of the solar wind speed as measured by the plasma experiment E1 on board *Helios-1*. (c) One-minute averages of the magnetic field magnitude as measured by the flux gate magnetometer E3 on board *Helios-1*. (d) Elevation angle and (e) azimuthal angle of the magnetic field in the Spacecraft Solar Ecliptic (SSE) coordinate system. (f) First-order (A_1/A_0) anisotropy along the magnetic field direction. (g) Second-order (A_2/A_0) anisotropy.

distributions were highly anisotropic, and the highest intensities were measured in those sectors pointing directly toward the Sun (Sectors 0 and 7). The vertical black lines (identified with the black arrows in Figure 2(a)) indicate the onset time of the SXR flare emissions prior subtraction of the ∼8.33 minutes that electromagnetic emissions take to propagate from Sun to Earth.

Figure 2(b) shows the solar wind speed as measured by the plasma experiment E1 on board *Helios-1* (Schwenn et al. 1975). Slow solar wind (∼250 km s^{-1}) was observed throughout all this period. Figure 2(c) shows the magnetic field magnitude as measured by the Flux Gate Magnetometer (experiment E3) on board *Helios-1* (Scearce et al. 1975), whereas Figures 2(d) and (e) show the elevation and azimuthal angle of the magnetic field vector in the Spacecraft Solar Ecliptic coordinate system. In this coordinate system the *X*-axis points from the spacecraft to the Sun, the *Z*-axis is normal to the ecliptic plane (positive northward) and the *Y*-axis completes the right-handed set. Figures 2(d) and (e) show that the magnetic field vector was essentially in the ecliptic plane and directed very close to the Sun-spacecraft radial direction. This

orientation allowed the observation of particle angular distributions with good coverage in pitch angle.

Traditionally (e.g., Balogh 1971; Sanderson et al. 1985, and references therein) particle anisotropies have been computed assuming that the PADs are gyrotropic in the plasma frame so that they can be expressed in terms of a truncated expansion of orthogonal Legendre polynomials as

$$F(\theta) = A_0 + A_1 \cos\theta + \frac{A_2}{2}(3\cos 2\theta - 1), \quad (1)$$

where θ is the particle pitch angle. The first-order anisotropy of the particle distribution is defined as the ratio between the first and the second coefficient of the expansion, A_1/A_0, which is related to the average mean pitch-angle cosine. The second-order anisotropy is given by A_2/A_0. A positive ratio of A_2/A_0, when the first-order coefficient is close to zero, represents a bidirectional contribution to the particle flows along the IMF. A large value of A_1/A_0 with $|A_1|>A_2$ represents a highly anisotropic flow of particles aligned with the IMF direction (see details of the procedure used to compute the anisotropy coefficients in, for example, Lario et al. 2001, and references therein).

We compute the first- and second-order anisotropy by fitting the function in Equation (1) to the eight sectored angular intensities measured by E6, where θ is the mean particle pitch angle observed by each sector (given by the central direction of each sector). Figures 2(f) and (g) show the evolution of the first- and second-order anisotropies, respectively. Figure 2(f) is directly comparable to Figure 5 of Kallenrode & Wibberenz (1991). Figures 2(f) and (g) show that the anisotropy attained its maximum value at the time of the intensity maximum and decayed shortly after that.

3. EXTRACTION OF RELEASE TIME HISTORIES

We use two different techniques previously used to infer the release time history of near-relativistic electrons at 1 au. The first technique, developed by Roelof (2008), is a data-driven method based on the assumption that the magnetic moment of the electrons is conserved during their interplanetary propagation between the Sun and the spacecraft and that there exists an effective process at some distance beyond the spacecraft able to reflect back the electrons in the sunward direction (Roelof 2008). The second technique is an inversion method that makes use of particle transport simulation results (Agueda et al. 2012) to fit the observations and infer the release time profile at the Sun and the interplanetary transport parameters. Both techniques rely on the information provided by in situ PADs.

3.1. Roelof (2008) Algorithm

Under the assumption that the electron magnetic moment is conserved between the Sun and the spacecraft, the differential intensity measured at a given spacecraft position, R_{SC}, after a particle injection from close to the Sun and for a given pitch-angle cosine μ can be written as (Roelof 2008)

$$j(\mu, t) = j_s(\mu_0, t - \tau(\mu, \mu_0)) + j(-\mu, t - 2\tau_m(\mu)) \quad \mu > 0, \quad (2)$$

where j_s is the injection intensity, μ_0 is the injection pitch-angle cosine near the Sun, and $\tau(\mu, \mu_0)$ is the transit time from the injection point to the observation point, R_{SC}, for the final and initial pitch-angle cosines (μ, μ_0). The pitch-angle cosines are inter-related by the conservation of the magnetic moment. Under the assumption that particles propagate scatter-free along the magnetic field line, we can approximate the particle transit time to

$$\tau(\mu, \mu_0) \sim \frac{z}{v}, \quad (3)$$

where v is the particle speed, z is the distance traveled by the particles along the magnetic field (assumed to be the length of the Parker spiral IMF line), and $\mu \approx 1$. The assumption of small particle pitch-angle considers that the strong focusing effect due to the large gradient of the IMF strength close to the Sun forces the particles to propagate nearly field-aligned, making the transit time independent of the injection pitch-angle cosine μ_0. Considering the observed solar wind speed of $\sim$250 km s^{-1}, the length of the IMF line connecting *Helios-1* to the Sun was $z \sim 0.32$ au. For a 490 keV electron with $\mu = 1$ the transit time from the Sun to the spacecraft along the IMF line was $\tau\sim$3.1 minutes (the energy 490 keV corresponds to the geometric mean of the energy window 300–800 keV).

Particles propagating inward (i.e., sunward) observed by the spacecraft with a given pitch-angle cosine $\mu < 0$ have a transit time

$$\tau_m \sim \mu\frac{z}{v} \quad (4)$$

to their mirroring point where they adiabatically change their sense of propagation to return (after a time $2\tau_m$) to the spacecraft's location R_{SC} with a pitch-angle cosine μ.

Under the supposition of the conservation of the electron's magnetic moment between the Sun and the observer, the observation of particles with $\mu < 0$ responds to back-scatter processes occurring at some distance beyond the observer's location (see Figure 1 in Roelof 2008). The particle detector at R_{SC} measures outgoing intensities (j_+) with $0 < \mu < 1$ and incoming intensities (j_-) with $-1 < \mu < 0$. The outgoing intensity is a mix of particles that were freshly released at the Sun (j_s), crossing the spacecraft location for the first time, together with those that crossed the observer's location previously (going inward with $\mu < 0$), mirrored at some inner distance $<R_{SC}$, and then crossed R_{SC} again with $\mu > 0$. The intensity of the outward-crossing particles can be expressed as $j_+(\mu, t)$. The intensity of particles that had inward-crossed at an earlier time, so that they could mirror and outward-cross R_{SC} at time t, can be expressed as $j_-(-\mu, t-2\tau_m)$. According to Equation (2), the injection history, $j_s(\mu, t)$, is then given by

$$j_s(\mu, t - \tau) = j_+(\mu, t) - j_-(-\mu, t - 2\tau_m). \quad (5)$$

Figure 3 shows the application of this technique to the four events observed by *Helios-1* at $R_{SC} = 0.31$ au. We have followed the same approach used by Roelof (2008) to extract the solar injection of 175–315 keV electrons observed by the Electron, Proton, and Alpha Monitor on the *Advanced Composition Explorer* (*ACE*) spacecraft (Gold et al. 1998) during the SEP event on 2000 February 18 (see their Figure 2). We use the 300–800 keV electron intensities j measured in the eight sectors of the E6 instrument as shown in Figure 2(a). The PADs obtained from this sectored data are approximated by the mathematical expressions $j_+(\mu, t) = j_{0+}(t)\exp(\alpha_+\mu)$ for the outgoing ($0 < \mu < 1$) and $j_-(\mu, t) = j_{0-}(t)\exp(\alpha_-\mu)$ for the

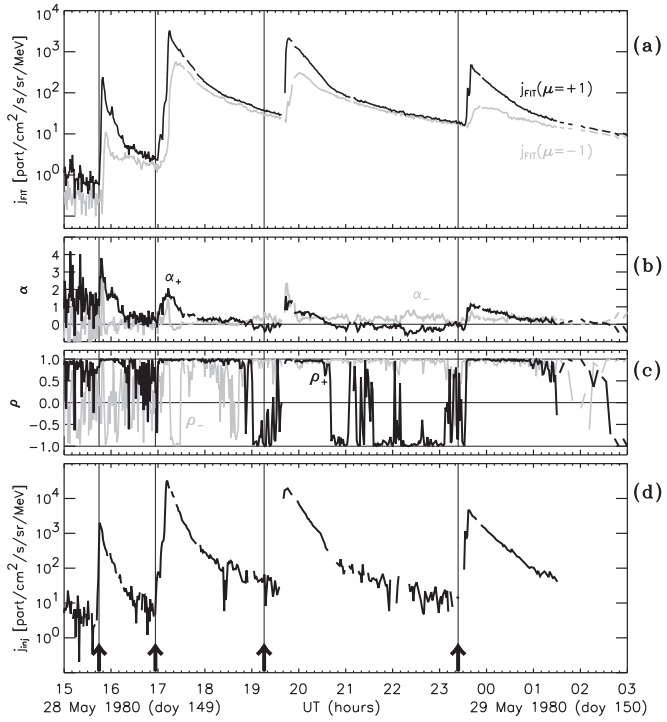

Figure 3. (a) $j_{\rm FIT}(\mu, t)$ and (b) α parameters obtained from fitting the pitch-angle distributions to the outgoing (black) and returning (gray) particles using the 300–800 keV electron intensities measured in the eight sectors of E6 as shown in Figure 2(a). (c) Linear Pearson correlation coefficient obtained from the fitting of the PADs of the outgoing (black) and returning (gray) particles. (d) Solar injection history for electrons with $\mu = 1$. Gaps in the solar injection function result from either actual gaps in the particle data or periods of time when the time resolution of the data does not allow us to have a data point near the estimated time $t - 2\tau_m$ in Equation (5). The vertical black lines and black arrows identify the onset of the SXR emissions shifted by 8.33 minutes.

returning ($-1 < \mu < 0$) electrons. Figure 3(a) shows the parameters j_+ at $\mu = 1$ (black) and j_- at $\mu = -1$ (gray) obtained from these fittings, whereas Figure 3(b) shows α_+ for the outgoing particles (black) and α_- for the returning particles (gray). Figure 3(c) shows the linear Pearson correlation coefficient, ρ, obtained from the fitting by the expression $\ln(j) \propto \alpha\mu$ to the outgoing (ρ_+, black) and returning (ρ_-, gray) particles. The E6 experiment provides only PAD information on eight sectors. Considering the IMF direction during this event (Figure 2(e)), only four sectors provide PAD information of the outgoing particle intensities and four for the returning particle intensities. The mathematical expression, $\exp(\alpha\mu)$, used to fit the observed PADs does not always provide a good fit to the four points describing the PADs of the outgoing and the four points of the returning particles. However, for the rising phases of the events, we see that ρ approaches unity, indicating that the function $\exp(\alpha\mu)$ is a good approximation, especially for the outgoing particles.

Figure 3(d) shows $j_s(\mu = 1, t)$ obtained applying Equation (2) shifted by the transit time of ~3.1 minutes for comparison with the solar electromagnetic emissions (the vertical black lines identified by the black arrows show the onset of the SXR emissions shifted by 8.33 minutes). Figure 3(d) shows that the onset of the injection for Events 2 and 4 coincided with the onset of the SXR emission. For Event 1 the inferred injection started two minutes before the onset of the SXR emission, whereas for Event 3 the inferred injection was delayed by $\gtrsim$19 minutes with respect to the onset of the SXR emission. It is worthwhile to point out that for Event 1 the microwave burst associated with the parent solar flare started before the SXR emission, peaking at 15:52 UT at the frequency 2.8 GHz; i.e., earlier than the SXR flare (see Table 2 in Gaizauskas (1983) and reports of microwave emissions[4]).

3.2. Inversion Methodology

We use the interplanetary transport model developed by Agueda et al. (2008) to simulate the propagation of 300–800 keV electrons from the Sun to the spacecraft. This model assumes that the particles propagate along IMF lines according to the diffusion-focused transport equation developed by Roelof (1969, p. 111) and expanded by Ruffolo et al. (1998). This equation includes the effects of particle streaming along the magnetic field lines, adiabatic focusing by the diverging magnetic field, interplanetary scattering by magnetic fluctuations frozen into the solar wind, convection with scattering fluctuations, and adiabatic deceleration resulting from the interplay of scattering and focusing. The model uses the Monte Carlo technique to compute the electron PADs at the spacecraft location resulting from a release at two solar radii. We assume that the spacecraft is located at $R_{\rm SC} = 0.31$ au and that it is connected with the Sun with an Archimedean IMF line determined by the solar wind speed measured in situ.

The results of the interplanetary transport model are computed in terms of Green's functions of particle transport, that is, PADs at the spacecraft location resulting from an instantaneous release at the Sun (see details in Agueda et al. 2014). We compute the Green's functions for different values of the radial mean-free path, λ_r, from 0.06 au to 1.20 au assuming that λ_r is independent of radial distance. The pitch-angle diffusion coefficient is assumed to be isotropic.

For comparison with the model results, the directional intensities at the spacecraft location were re-binned assuming 10 bins in pitch-angle cosine using the expression $e^{\alpha\mu}$ over the eight sectors and assuming one-minute time resolution (see Figure 4). Figure 5(a) shows the time-intensity profiles resulting from this re-binning, whereas Figure 5(b) shows the quality of the fitting using the expression $e^{\alpha\mu}$ over the eight sectors (see also Figure 4). We marked the time period selected for fitting for each event with gray rectangles. It can be seen that during the rising phase and until the end of these time intervals the Pearson correlation coefficient was close to 1 and the exponential $e^{\alpha\mu}$ was a good description of the PADs.

We use an inversion approach to extract the electron release time profile at the Sun, $q(t)$. The modeled PADs, M_j, resulting from a series of impulse solar injections can be written as

$$M_j(t; \lambda) = \int_{T_1}^{T_2} dt' g_j(t, t'; \lambda) q(t'), \quad (6)$$

where $g_j(t, t'; \lambda)$ represents the impulse response in a given pitch angle j, at a given time t, when particle injection took place at time t' and assuming an interplanetary mean-free path λ. The duration of the injection function, $t' \in [T_1, T_2]$, is determined by the SEP event time interval selected for fitting, $t \in [t_1, t_2]$, that is, $T_1 = t_1 - \Delta t$ and $T_2 = t_2 - \Delta t$, where Δt is the transit time of the first arriving particles at the spacecraft location, for a given value of the scattering mean-free path. The

[4] ftp.ngdc.noaa.gov/STP/space-weather/solar-data/solar-features/solar-radio/radio-bursts/reports/

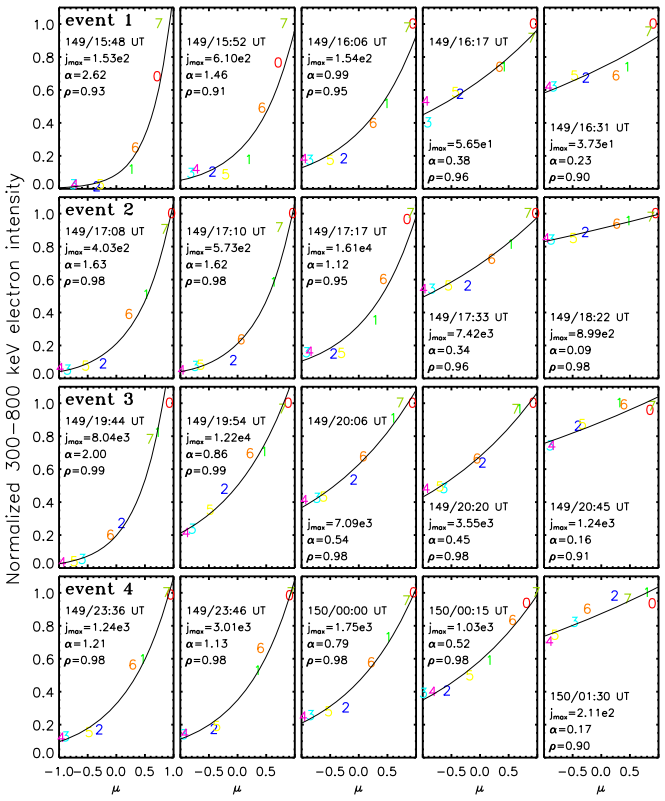

Figure 4. Observational sectored intensities (colored numbers from 0 to 7) normalized to the intensity measured in the sector with maximum number of counts ($j_{\max}$) as a function of the pitch-angle cosine μ for five snapshots of each event. The values of $j_{\max}$ listed in each panel are in units of counts $(\mathrm{cm^2\ s\ sr\ MeV})^{-1}$. The thin black traces show the least-squares fit using the expression $e^{\alpha\mu}$. The values of α and the linear Pearson correlation coefficient ρ obtained from the fit are listed in each panel.

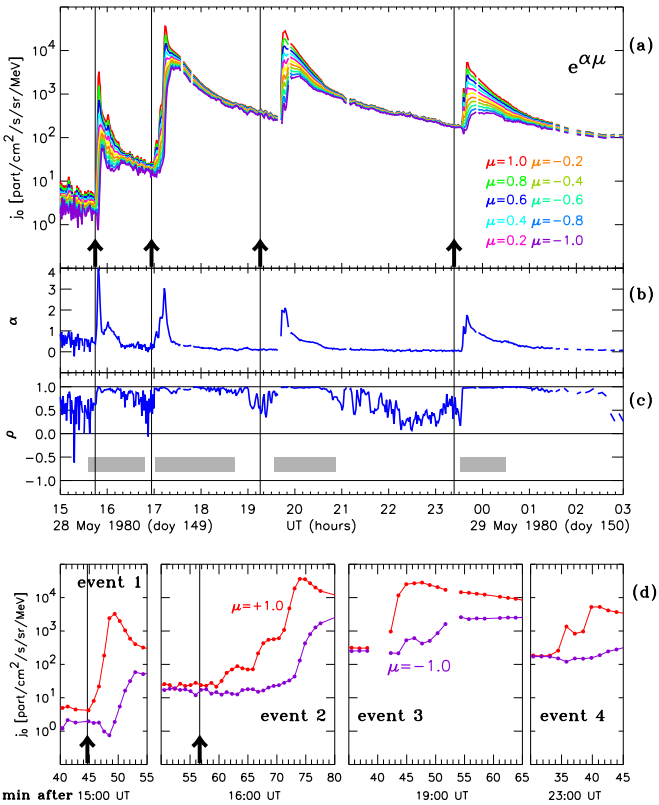

Figure 5. (a) One-minute averages of the 300–800 keV electron intensity time profiles at specific pitch-angle cosines assuming that the PADs shown in Figure 2(a) can be approximated by $j = j_0 e^{\alpha\mu}$. (b) Values of α obtained from fitting the PADs formed by the eight sectors of E6. (c) Linear Pearson correlation coefficient. The gray rectangles show the time period selected for modeling in Section 3.2. (d) Time-intensity profiles at pitch-angle cosine $\mu = 1$ (red) and $\mu = -1$ (purple) at the onset of the events.

number of time points in the event time interval selected for fitting is equal to $n_t = (t_2 - t_1)/\delta t + 2$, where δt is the time resolution of the data.

Let J_i be the observations (pre-event background subtracted). We want to derive the n_t-vector $\boldsymbol{q}$ that minimizes the length of the vector $\boldsymbol{J} - \boldsymbol{M}$. That means minimizing the value of

$$||\boldsymbol{J} - \boldsymbol{M}|| \equiv ||\boldsymbol{J} - \boldsymbol{g} \cdot \boldsymbol{q}||, \quad (7)$$

subject to the constraint that $q_l \geqslant 0 \quad \forall l = 1, 2, \ldots, n_t$. We obtain the injection amplitudes using the non-negative least-squares method developed by Lawson & Hanson (1974), which always converges to a solution. The value of the electron interplanetary mean-free path is determined by estimating for which of the tested λ_r-values the discrepancy between the observed and the modeled intensities is smallest (see Agueda et al. 2008, 2014, for more details). The goodness-of-fit estimator computes the sum of logarithmic differences between the observational and the modeled data.

Figure 6 shows the values of the goodness-of-fit estimator obtained for the range of λ_r-values tested (between 0.06 and 1.20 au). A clear minimum of the goodness-of-fit estimator was found in all events. Figure 7 shows the observed electron intensities (dotted symbols) for the four events and the simulated electron intensities (black traces) for the best fits. The best fits can mostly reproduce the observations, i.e., the evolution of the PADs, and the omni-directional- and first-order anisotropy-time profiles. Some discrepancies between the data

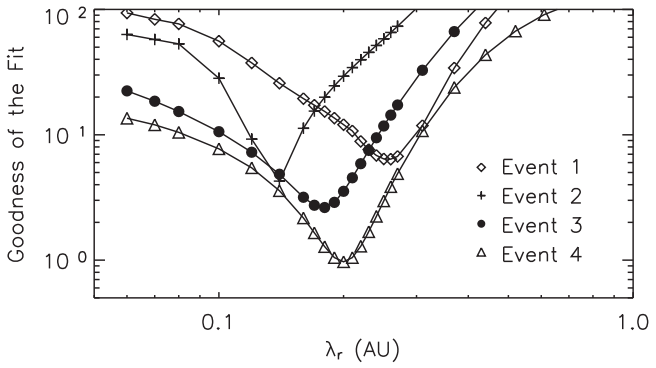

Figure 6. Goodness of the fit for the four events observed by *Helios-1* on 1980 May 28.

and the model appear for negative pitch-angle cosines. In any case, the aim was to reproduce the overall time evolution of the PADs, which contains more information than the average intensity time profile and the first-order anisotropy combined.

Column 2 of Table 2 lists the mean-free paths obtained with the inversion method for each event. The obtained values of λ_r range between 0.26 au (Event 1) and 0.14 au (Event 2), being 0.18 and 0.20 au for Events 3 and 4. Column 3 of Table 2 gives the ratio between the particle mean-free path λ and the distance z of the observer along the Archimedean spiral as a crude criterion to distinguish between diffusive ($\lambda/z \leqslant 1/5$), focused ($1/5 < \lambda/z \leqslant 1$), and scatter-free ($\lambda/z > 1$) propagation

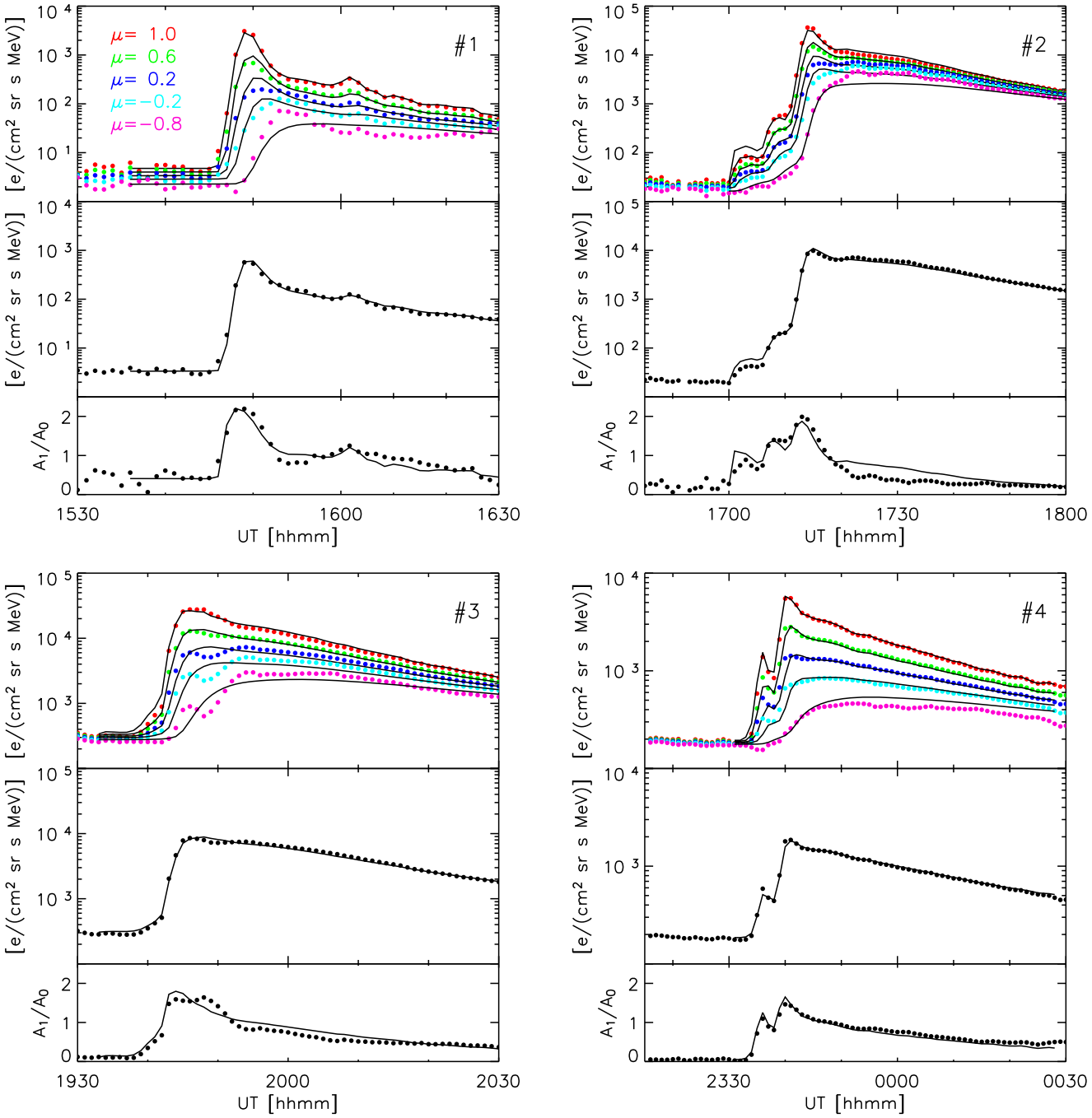

Figure 7. For each event and from top to bottom: Electron 300–800 keV PADs (shown for five pitch-angle cosines), omni-directional intensities, and first-order anisotropy. Data are shown by dots and the model predictions are shown with black curves.

(Kallenrode & Wibberenz 1991). The mean-free paths derived in this study suggest that electrons propagated in the focused regime. This can also be seen in the PADs (Figure 7), i.e., the large anisotropy at the time of maximum indicates that the scattering was not too strong for these events, but the decay phase shows that the events were not pure scatter-free.

4. INFERRED PARTICLE INJECTIONS

The time profiles of the electron release histories inferred using the two techniques are displayed in Figure 8. The histograms show the results obtained with the inversion method described in Section 3.2, whereas the solid thick lines show the injection profiles using the technique described in Section 3.1. The general characteristics of the profiles inferred using the two techniques are similar early in the event (up to the time of the intensity maximum), when the influence of interplanetary propagation is small. For all the events, the intensities for $\mu = -1$ reach values at least one order of magnitude smaller than for $\mu = 1$, and they start to rise mostly after the time of the intensity maximum in $\mu = 1$ (Figure 5(d)). Therefore, the rise phase of the intensity time profile observed for $\mu = 1$ shifted in time by the transit time along the IMF can be used to estimate the beginning of the solar release time profile. The total number of electrons injected per unit solid angle at the solar wind source surface can be estimated by integrating the release time

Table 2
Transport and Release Parameters

	Transport		Release Parameters			
	Parameters		Inversion Method		Roelof (2008) Algorithm	
Event #	λ_r (au)	λ/z	Peak (UT)	Max. Int. (e/(s sr MeV))	Peak (UT)	Max. Int. (e/(cm^2 s sr MeV))
1	0.26	1/1.2	15:46	5×10^{29}	15:45	2×10^{3}
2	0.14	1/2.3	17:11	1×10^{31}	17:11	33×10^{3}
3	0.18	1/1.8	19:42	6×10^{30}	19:46	19×10^{3}
4	0.20	1/1.6	23:37	1×10^{30}	23:38	4×10^{3}

profile obtained with the inversion method. By re-normalizing the release time profile obtained with the Roelof (2008) algorithm, we obtain that the two methods differ in the total number of particles released, being this about two times larger when interplanetary propagation is ignored.

Columns 4 and 5 of Table 2 list the injection parameters (peak times and maximum value) inferred with the inversion method described in Section 3.2, whereas columns 6 and 7 show the same parameters for the Roelof (2008) method described in Section 3.1. The largest release in terms of number of particles was associated with Event 2; it expanded three orders of magnitude during 1.5 hr. The smallest release, lasting only 15 minutes, was associated with Event 1. Event 3 and Event 4 had comparable releases in terms of duration ($\gtrsim$1 hr), with the release for Event 3 reaching a little higher instensity. The profiles for Event 2 and 4 show a double peak structure during the rising phase of the profile. The double peak structure was reported for particle and electromagnetic data for Event 2, the largest of the four events, in Kallenrode & Wibberenz (1991).

For comparison with the solar electromagnetic emissions, the vertical red lines in Figure 8 show the start, maximum, and end time (in some cases) of the SXR emission shifted by 8.33 minutes. For the large events (2, 3, and 4) the maximum of the SXR emission coincides with the peak in particle release. For the shortest flare (Event 1) the maximum in SXR emission was four minutes delayed with respect to the peak in particle release. It is worthwhile pointing out that for this event the microwave burst associated with the parent solar flare started before the SXR, peaking at 15:52 UT (15:44 UT after 8 minutes subtraction) at the frequency 2.8 GHz.

The beginning of the release coincided with the onset of the SXR emission for Events 1 and 2. For Events 3 and 4, the beginning of the inferred release was delayed with respect to the onset of the SXR emission by 20 and 6 minutes, respectively. This could be related to the fact that these events were observed during periods of high background intensities due to previous events, allowing for the possibility that the first released particles remained below background.

5. DISCUSSION

In a sample of four consecutive relativistic electron events observed in the inner heliosphere, we found that the amount of interplanetary scattering varies from one event to the other. We obtained values of the radial mean-free path in the range from 0.14 to 0.26 au, corresponding to parallel mean-free paths $\lambda_{||}$ of 0.55 and 1.02 au at the orbit of the Earth. Figure 9 (top panel) shows the radial mean-free path versus the maximum intensity of particle release for each event. From this set of events, we find indications that the strength of the scattering varies systematically with the amount of electrons released by the solar parent event, which suggests that the magnetic field fluctuations leading to interplanetary scattering are not necessarily an inherent property of the interplanetary medium, but they are related to the amount of released particles at the Sun. The amplification of turbulence by streaming energetic particles was observed by Kurt et al. (1977) for non-relativistic electrons, and it has also been suggested for protons (Reames 1989). By contrast, Kallenrode et al. (1992) found no marked indication that the strength of scattering varied systematically with the size of the particle event. In their analysis they included mean-free path values inferred for events observed at different sites within 1 au, and normalized the maximum intensity of the particle event to an observer site at 1 au using simplified radial scaling laws.

A puzzling feature is the large variation of mean-free path values obtained using conventional models of SEP transport. For example, most small SEP events exhibit "scatter-free" propagation characteristics, while small diffusive events have not been reported. *Helios* observations provided us with a sample of scatter-free electron events observed close to the Sun (see Kunow et al. 1991). This was interpreted as a signature that pure scatter-free propagation might occur exclusively close to the Sun. Another interpretation is that as we approach the Sun, we are able to observe SEP events produced by weaker sources that occur under essentially scatter-free propagation conditions due to small self-generated turbulence.

Figure 9 (bottom panel) shows the radial mean-free path versus the time delay between peak intensities of consecutive release time episodes, as inferred from Figure 8. From this set of four events, the strength of the scattering varies systematically with the time delay between releases. The larger the delay, the larger the mean-free path, suggesting that particles streaming along the magnetic field may excite turbulence, which then decays with a characteristic time constant. It is also remarkable that from event #1 to event #2 the mean-free path changes its value by a factor of two within approximately 90 minutes. This time is much smaller than the time it takes the solar wind to propagate to 0.3 au (~50 hr at 250 km s^{-1}), and even smaller than the typical duration of solar energetic electron events (a few hours). Therefore it seems plausible that the value of the mean-free path varies substantially during the course of an event.

A comparison between the solar electron release time histories obtained using a data-driven method and a simulation-based technique allows us to conclude that the early phase (up to the maximum) of the release history of SEP can be reliably studied assuming scatter-free propagation in the inner heliosphere. This is in agreement with Kallenrode &

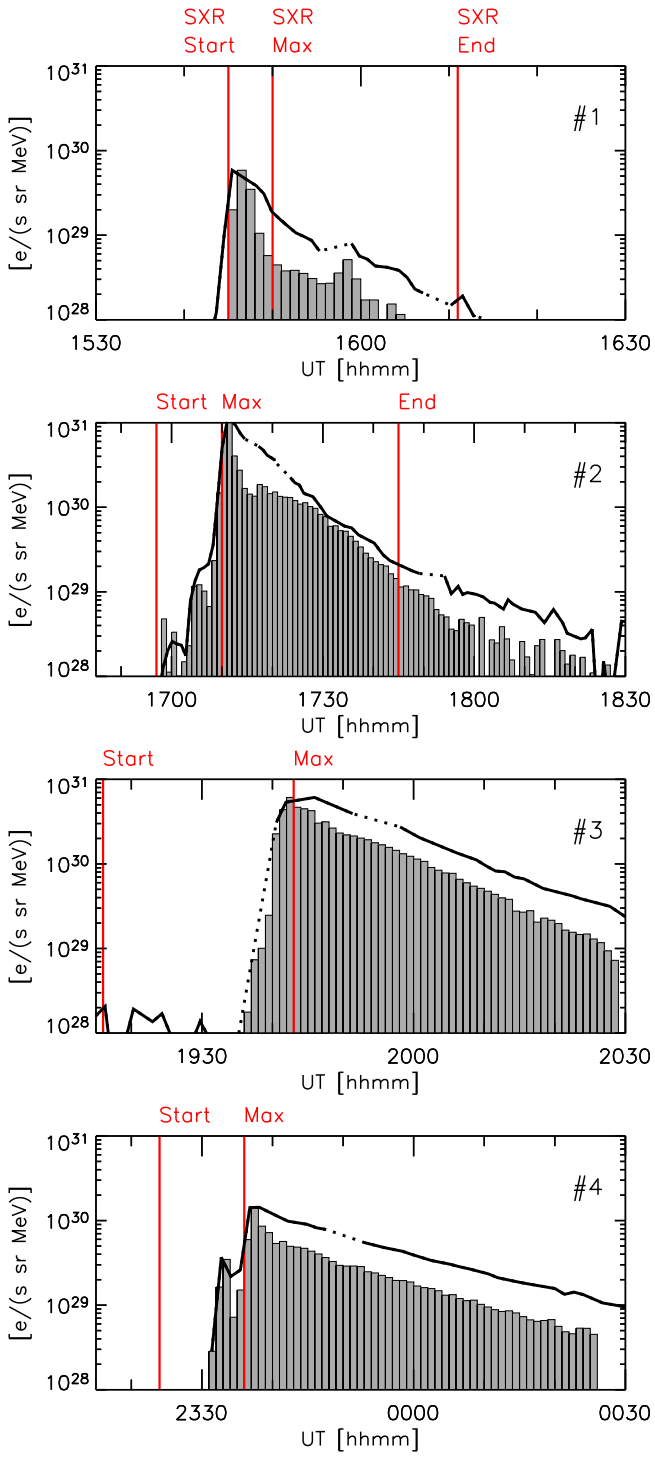

Figure 8. Release time profiles inferred for the four events. The histograms show the inversion results with one-minute time resolution. The black thick curves show the results extracted using the algorithm of Roelof (2008) re-normalized to the inversion result maximum. The vertical red lines show the start, maximum, and end time (in some cases) of the SXR emission shifted by 8.33 minutes.

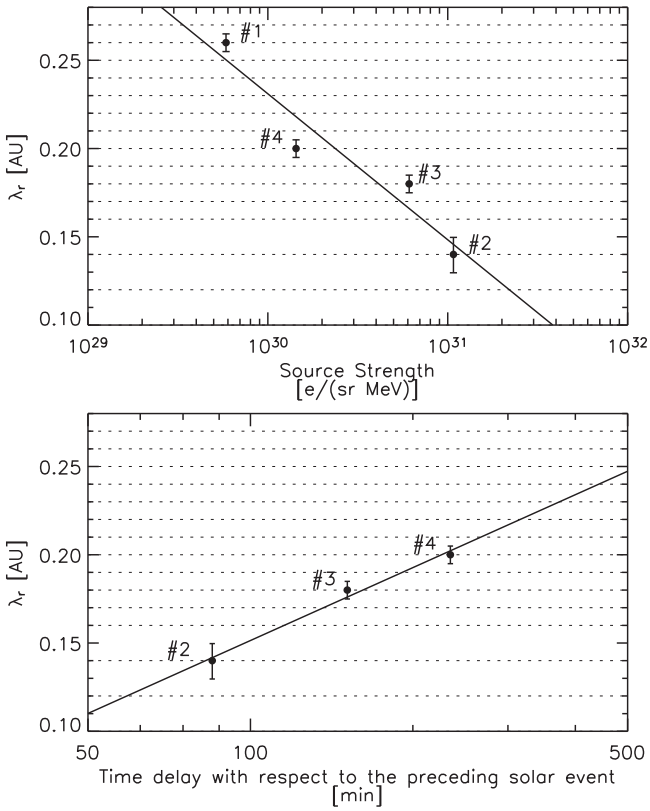

Figure 9. Mean-free path λ_r vs. maximum intensity of particle release (top panel) and time delay with respect to the preceding solar release (bottom panel) for the four events under study. The solid line shows a linear fit. The horizontal dotted lines mark the resolution of the grid in λ_r. Error bars show an estimate of the uncertainty in λ_r.

Wibberenz (1990) and it makes it possible to extract the early release time history directly from data without any propagation modeling. In principle, such an extraction could be carried out in real time directly from the data acquired by spacecraft. However, it is essential to have a good coverage in pitch angle to build reliable PADs especially during the onset, rising, and maximum phases of SEP events. Future non-spinning spacecraft, such as the *Solar Orbiter* and *Solar Probe Plus*, will measure SEP angular distributions with limited fields of view, missing the sunward direction where particles with small pitch angles tend to be focused in case of nearly radial magnetic field. It is thus imperative to develop techniques to reconstruct the PADs from the observations to estimate the intensities for $\mu = 1$ and $\mu = -1$. As shown in Figures 5(d) and 7, the intensity time profiles at different pitch angles can be completely different, and a given event can be interpreted differently if we cannot observe particles arriving at the spacecraft with small pitch angles (see e.g., Agueda et al. 2009b). Limited pitch-angle coverage might result in inferring erroneous release time histories.

We now address the fact that *IMP-8* observed apparently only a single electron intensity increase during this time interval (Wibberenz & Cane 2006). As pointed out by McComas et al. (2014), the observation of a single smeared SEP event at 1 au could result from a combination of one or more of the following processes: (1) distinct magnetic connections of the spacecraft to the particle source(s); (2) the spatio-temporal evolution of the particle sources; and (3) scattering and diffusion during transport from 0.31 to 1 au.

Based on the release time profiles we inferred from *Helios-1* data in Section 3.2, we can use the interplanetary transport model to compute the intensity time profiles that a hypothetical observer located at 1 au would observe. We compute the connection angle of *IMP-8* with the four parent flares and estimate the maximum electron release expected at the *IMP-8*'s

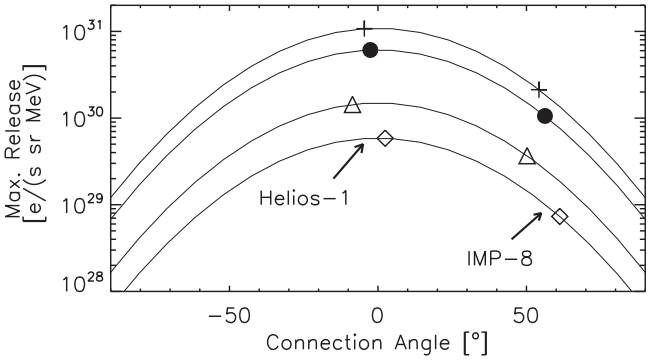

Figure 10. Variation of maximum release intensities with connection angle. Amplitudes for the same event are marked by the same symbols (as in Figure 2) and connected by a Gaussian distribution centered at zero longitude, with standard deviation $\sigma = 30°$. Assuming this variation with connection angle for the four events, the maximum release at *IMP-8*'s footpoint would be about one order of magnitude smaller than the one inferred in Section 4 for the *Helios-1* footpoint.

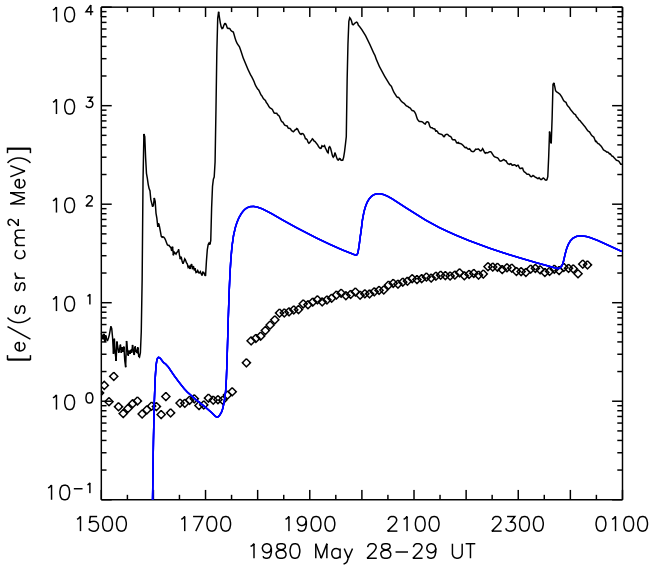

Figure 11. Electron 300–800 keV intensities observed at 0.31 au by *Helios-1* (solid black curve). Intensities expected at 1 au (blue curves) assuming the same interplanetary transport conditions and the same injection histories deduced for *Helios-1* scaled according to a Gaussian distribution centered at the source region (see text for details). Electron 220–800 keV intensities observed by *IMP-8* at 1 au (black diamonds).

flux tube by assuming that the particle source intensity follows a Gaussian distribution centered at the flare site with standard deviation $\sigma = 30°$ (see Figure 10), following the results by Wibberenz & Cane (2006). Assuming this variation with connection angle for the four events, the maximum release at *IMP-8*'s footpoint would be about one order of magnitude smaller than the one inferred in Section 4 for the *Helios-1* footpoint. Figure 11 shows the 300–800 keV electron intensity time profiles resulting at 1 au under the assumption that the same time evolution of particle release and the same transport conditions deduced to fit the *Helios-1* observations are valid between 0.31 and 1 au. Under these two assumptions, an observer at 1 au would still observe four separated intensity enhancements with intensities larger than those measured by *IMP-8*.

By contrast, *IMP-8* observed only a single gradual electron enhancement (diamond symbols in Figure 11). The Charged Particle Measurement Experiment (Sarris et al. 1976) on board *IMP-8* provides electron sectored data but only in the energy channel 0.22–2.5 MeV. With the exception of an unfortunate data gap of ∼15 minutes at the onset of the event (between 17:30 and 17:44 UT), intensities in the different sectors were very similar (not shown here), indicating that isotropic fluxes were observed throughout the event.

Uncertainties about (i) the magnetic connection of the spacecraft with the Sun, (ii) the factor used to scale with connection angle the injection for *IMP-8*, (iii) the time profile assumed for the release of electrons onto the IMF line connecting *IMP-8* with the Sun, and (iv) the transport conditions along this IMF line would allow us to find an intensity time profile at 1 au that mimics the observations; however, we decided to keep unsustainable assumptions to a minimum. A common result from the study of near-relativistic electron events observed by spacecraft widely separated in longitude (including *STEREO*, *ACE*, and *Ulysses* observations) is that the release time profile is different for different connection angles (Agueda et al. 2012; Gómez-Herrero et al. 2015). For footpoints closer to the source region, the timing of the maximum release is more in accordance with the peak in SXR emission, while for distant footpoints the release starts later in time and follows a ramp-like profile that reaches lower intensities. Therefore, it is reasonable to assume that the release of particles observed by *IMP-8* did not follow the same time history as those observed by *Helios-1*.

Moreover, Event 1 was the smallest in terms of the number of injected electrons (Table 2) being reasonable to assume that the source for this event was narrow and hence that this event was not observed by the poorly connected *IMP-8* spacecraft. By contrast, Event 2 was the largest in terms of the number of injected electrons (Table 2) and most likely the particle source was broader in longitude being most likely to be observed by *IMP-8*. The subsequent smaller Events 3 and 4, in terms of number of electrons (Table 2) and possibly with narrow particle sources, contributed only a small amount to the already enhanced *IMP-8* intensity profile.

Another possibility would be that interplanetary scattering processes are more prominent beyond the *Helios-1* orbit. Kallenrode et al. (1992) showed that it is difficult to distinguish a radially constant mean-free path and a moderate radial variation such as $\lambda_r = \lambda_0 (r/r_0)^b$ with $b = -1$. The main difference between the two scenarios is in the intensity onset and maximum, leading the radial-dependent λ_r to a faster intensity increase and a "sharper" maximum (Kallenrode et al. 1992). Since the intensities observed by *IMP-8* are more gradual than the profiles predicted assuming a radially constant mean-free path, the assumption of $b = 0$ seems to be reasonable. In addition, the decay phase of the electron events at 0.31 au is nicely modeled. Additional explanations for the observation of a single time-extended event by *IMP-8* include a variation of λ_r with heliolongitude (more particle scattering on field lines connecting to *IMP-8*), and the possibility that the majority of the electrons reached the field lines connecting to *IMP-8* by diffusion perpendicular to the heliospheric magnetic field that can explain the isotropic character of the event at 1 au

(Dröge et al. 2010; Strauss & Fichtner 2015; Laitinen et al. 2016).

6. CONCLUSIONS

For a group of four consecutive relativistic electron events observed by *Helios-1* on 1980 May 28 we find the release time history at the Sun using two different techniques. The first one assumes conservation of the magnetic moment as electrons propagate in the inner heliosphere between the Sun and the observer. The second one considers interplanetary scattering by using the results of a transport model to fit the observations. Both techniques make use of the PADs to extract the accurate release time history of electrons. PADs measured in different regions of the heliosphere are essential to determine the processes of particle acceleration at the Sun and deconvolve the SEP transport effects.

We infer interplanetary transport conditions for the four events in the range of focused transport, with values of λ_r from 0.14 to 0.26 au. The mean-free path obtained for each event scales systematically with the strength of the particle release, which suggests that the magnetic field fluctuations leading to interplanetary scattering might be related to the amount of released particles at the Sun. In addition, the strength of the scattering varies systematically with the time delay between releases, which suggests that particles streaming along the magnetic field may excite turbulence, which then decays with a characteristic time constant.

The release time profiles obtained with the two methodologies are very similar, especially up to the time of the maximum. This is due to the small influence of interplanetary propagation on the early phase of SEP events at radial distances smaller than 0.5 au.

An analysis of the single relativistic electron event observed by *IMP-8* on the same date at 1 au indicates that the dramatically different time-intensity profiles observed by the two spacecraft could result from a combination of one or more of the following processes: (1) distinct magnetic connections of the spacecraft to the particle sources; (2) the spatio-temporal evolution of the particle sources; and (3) scattering and diffusion during interplanetary transport, including the effects of a radial and heliolongitude dependence of λ_r as well as processes of perpendicular transport to the IMF.

Future non-spinning spacecraft, such as the *Solar Orbiter* and *Solar Probe Plus*, will measure SEP angular distributions with only a limited number of fields of view. It is thus imperative to develop techniques to reconstruct the PADs from the observations.

N.A. acknowledges financial support by the Spanish MINECO under project AYA2013-42614-P, MDM-2014-0369 of ICCUB (Unidad de Excelencia "María de Maeztu") and the European Union under grant agreement No. 637324 (HESPERIA). D.L. acknowledges the support from NASA under grants NNX11A083G, NNX15AD03G, and NNX16AF73G. We thank B. Heber and J.J. Blanco for providing the Helios-1 data used in this work. The present work benefited from discussions held at the International Space Science Institute (ISSI, Bern, Switzerland) within the frame of the international teams Exploration of the inner Heliosphere: what we have learned from *Helios* and what we want to study with *Solar Orbiter* led by Dr. W. Dröge, and The Connection Between Coronal Shock Wave Dynamics and Early SEP Production led by Dr. K. Kozarev and Dr. N. Nitta.

REFERENCES

Agueda, N., Klein, K.-L., Vilmer, N., et al. 2014, A&A, 570, A5
Agueda, N., Lario, D., Ontiveros, V., et al. 2012, SoPh, 281, 319
Agueda, N., Lario, D., Vainio, R., et al. 2009a, A&A, 507, 981
Agueda, N., & Vainio, R. 2013, JSWSC, 3, A10
Agueda, N., Vainio, R., Lario, D., & Sanahuja, B. 2008, ApJ, 675, 1601
Agueda, N., Vainio, R., Lario, D., & Sanahuja, B. 2009b, AdSpR, 44, 794
Agueda, N., Vainio, R., & Sanahuja, B. 2012, ApJS, 202, 18
Balogh, A. 1971, P&SS, 19, 533
Beeck, J., Mason, G. M., Hamilton, D. C., et al. 1987, ApJ, 322, 1052
Bialk, M., Dröge, W., & Heber, B. 1991, ICRC, 3, 764
Dröge, W. 2003, ApJ, 589, 1027
Dröge, W., Kartavykh, Y. Y., Klecker, B., & Kovaltsov, G. A. 2010, ApJ, 709, 912
Earl, J. A. 1974, ApJ, 193, 231
Earl, J. A. 1976, ApJ, 205, 900
Fox, N. J., Velli, M. C., Bale, S. D., et al. 2015, SSRv, in press
Gaizauskas, V. 1983, AdSpR, 2, 11
Gold, R. E., Krimigis, S. M., Hawkins, S. E., III, et al. 1998, SSRv, 86, 541
Gómez-Herrero, R., Dresing, N., Klassen, A., et al. 2015, ApJ, 799, 55
Gopalswamy, N. 2012, in AIP Conf. Ser. 1436, Physics of the Heliosphere: A 10 Year Retrospective (Melville, NY: AIP), 247
Hamilton, D. C. 1977, JGR, 82, 2157
Kahler, S., Burkepile, J., & Reames, D. 1999, ICRC, 6, 248
Kallenrode, M.-B. 1989, PhD thesis, Univ. Kiel
Kallenrode, M.-B., & Wibberenz, G. 1990, ICRC, 5, 229
Kallenrode, M.-B., & Wibberenz, G. 1991, ApJ, 376, 787
Kallenrode, M.-B., Wibberenz, G., & Hucke, S. 1992, ApJ, 394, 351
Kocharov, L., Vainio, R., Kovaltsov, G. A., & Torsti, J. 1998, SoPh, 182, 195
Kunow, H., Wibberenz, G., Green, G., Müller-Mellin, R., & Kallenrode, M.-B. 1991, Physics of the Inner Heliosphere II, vol. 152 (Berlin: Spring)
Kunow, H., Witte, M., Wibberenz, G., et al. 1977, JGZG, 42, 615
Kurt, V. G., Logachev, I. I., & Pissarenko, N. F. 1977, SoPh, 53, 157
Laitinen, T., Dalla, S., & Marsh, M. S. 2013, ApJL, 773, L29
Laitinen, T., Klein, K.-L., Kocharov, L., et al. 2000, A&A, 360, 729
Laitinen, T., Kopp, A., Effenberger, F., Dalla, S., & Marsh, M. S. 2016, A&A, 591, A18
Lario, D., Haggerty, D. K., Roelof, E. C., et al. 2001, SSRv, 97, 277
Lawson, C. L., & Hanson, R. J. 1974, Solving Least Squares Problems (Englewood Cliffs, NJ: Prentice-Hall)
McComas, D. J., Alexander, N., Angold, N., et al. 2014, SSRv, in press
McComas, D. J., Velli, M., Lewis, W. S., et al. 2007, RvGeo, 45, RG1004
Müller, D., Marsden, R. G., St., Cyr, O. C., & Gilbert, H. R. 2013, SoPh, 285, 25
Qin, G., Zhang, M., Dwyer, J. R., Rassoul, H. K., & Mason, G. M. 2005, ApJ, 627, 562
Reames, D. V. 1989, ApJL, 342, L51
Reid, G. C. 1964, JGR, 69, 2659
Roelof, E. C. 1969, Lectures in High-Energy Astrophysics, ed. H. Ögelman & J. R. Wayland (Washington, DC: NASA), 111
Roelof, E. C. 1975, ICRC, 5, 1716
Roelof, E. C. 1979, GMS, 21, 220
Roelof, E. C. 2008, in AIP Conf. Ser. 1039, Particle Acceleration and Transport in the Heliosphere and Beyond, ed. G. Li et al. (Melville, NY: AIP), 174
Ruffolo, D. 1995, ApJ, 442, 861
Ruffolo, D., Khumlumlert, T., & Youngdee, W. 1998, JGR, 103, 20591
Sanderson, T. R., Reinhard, R., van Nes, P., & Wenzel, K.-P. 1985, JGR, 90, 19
Sarris, E. T., Krimigis, S. M., & Armstrong, T. P. 1976, JGR, 81, 2341
Scearce, C., Ness, N., Burlaga, L., et al. 1975, RF, 19, 237
Schulze, B. M., Richter, A. K., & Wibberenz, C. 1977, SoPh, 54, 207
Schwenn, R., Rosenbauer, H., Miggenrieder, H., et al. 1975, RF, 19, 226
Strauss, R. D., & Fichtner, H. 2015, ApJ, 801, 29
von Rosenvinge, T., & Cane, H. V. 2006, GMS, 165, 103
Wang, L., Lin, R. P., Krucker, S., & Gosling, J. T. 2006, GeoRL, 33, L03106
Wibberenz, G., & Cane, H. V. 2006, ApJ, 650, 1199
Wibberenz, G., Kunow, H., Iwers, B., Kecskemety, K., & Somogyi, A. 1989, SoPh, 124, 353